



Modeling spontaneous adiabatic shear band formation in electro-magnetically collapsing thick-walled cylinders



Z. Lovinger^{a,b,*}, D. Rittel^a, Z. Rosenberg^b

^a Technion – Faculty of Mechanical Engineering, Technion, Haifa 32000, Israel

^b RAFAEL, P. O. B 2250, 21031, Israel

ARTICLE INFO

Article history:

Received 19 July 2016

Available online 31 January 2017

ABSTRACT

The ability to simulate shear bands evolution in thick-walled-cylinder (TWC) experiments is required to understand their spontaneous formation and propagation. Recently we presented experiments on electro-magnetically collapsing metallic cylinders (Lovinger et al., 2015). Here we present numerical simulations that reproduce the experimental results for multiple shear bands in those TWC's. We present a detailed study of the initiation and propagation of the shear bands and their mutual interactions, which replicates many of the experimental observations. We investigate the influence of initial perturbations and pressure history on the initiation and final stages of the process using an energy-based failure model which incorporates a positive feedback mechanism. The numerical model is calibrated for four different materials to reconstruct the number of shear bands and their experimentally determined distribution. The results indicate that the number of shear bands is related to deformation micromechanisms operating in the material, such as twinning and martensitic transformations, which may hold back and eventually stall the shear bands evolution. The numerical simulations provide a reliable quantitative description of the shear bands distribution and spacing, thus paving the way for future predictive work of this failure mode.

© 2017 Elsevier Ltd. All rights reserved.

1. Introduction

Modeling adiabatic shear banding (ASB) has been a standing issue for the past few decades. As shear localization is an important and often dominant failure mode at high strain rates, as well as a precursor to catastrophic failure, a reliable predictive capability is highly desirable. Such a modeling capability should faithfully represent the mechanics and the physics of the dynamic material behavior. ASB formation in a dynamically loaded metal is traditionally viewed as a structural and/or material instability. The strength of a material is considered to be controlled by two competing mechanisms: hardening, such as strain and strain-rate hardening, and softening such as thermal (Zener and Hollomon, 1943) and microstructure-related softening (Rittel et al., 2006, 2008; Osovski et al., 2012). The classical approach of Zener and Hollomon (1943), which was recently reported (Dodd et al., 2015) to have been presented earlier by Kravz-Tarnavskii (1928) and Davidenkov and Mirolubov (1935), relates the initiation of adiabatic shear localization to the dominance of the thermal softening over the hardening mechanisms. Namely, under high rate deformation, the thermal softening results in a loss of strength leading to a feedback

mechanism between the plastic work and the consequent decrease in flow stress. In the last decade, an alternative process was proposed for ASB formation (Rittel et al., 2006, 2008; Osovski et al., 2012), identifying microstructural evolution (e.g. dynamic recrystallization) as the dominant softening mechanism. In these works, the dynamic stored energy of cold work was identified as the driving force for shear localization, which is, in fact, preceded and triggered by dynamic recrystallization (Rittel et al., 2006).

For each approach, a constitutive model that could capture the formation and evolution of adiabatic shear banding has to include a localization criterion and a positive feedback mechanism, due to the mutual relation between plastic work and material softening (either thermal or microstructural). In addition, such a model should express the dependence on material thermo-mechanical and/or microstructural properties, in order to account for the susceptibility of materials to shear banding, and the different ASB characteristics in various materials as observed experimentally.

We recently presented an experimental study on the spontaneous evolution of adiabatic shear bands in collapsing Thick Walled Cylinders (TWC) (Lovinger et al., 2015, 2011). As detailed and explained in Lovinger et al. (2011), the examination of spontaneous adiabatic shear bands highlights the inherent susceptibility of a material to adiabatic shear banding, without any geometrical constraint related to stress concentrations. Following our

* Corresponding author at: Technion, Haifa 32000, Israel.
E-mail address: cvloving@gmail.com (Z. Lovinger).

experimental work, as well as other works on explosively driven TWCs (Xue et al., 2004, 2002; Meyers et al., 2003; Yang et al., 2008, 2009), we aim at modeling the formation and evolution of multiple adiabatic shear bands in TWCs, with the inherent complexity related to the mutual interactions between the shear bands during their growth. The number of shear bands and their spatial distribution, as well as the conditions prevailing at their onset of formation, as characterized in Lovinger et al. (2011), provide a large database to select a proper constitutive model together with a failure criterion, for different materials.

Numerical modeling of spontaneous shear band evolution, in TWC tests, is pursued in the literature through either 1D or 2D/3D modeling of shear bands. The 1D modeling follows different strength and failure models, in order to predict the spacing between shear bands (e.g. Grady, 1982; Wright and Okendon, 1996; Molinari, 1997; Daridon et al., 2004). 2D/3D numerical simulations are aimed at reproducing the formation and evolution of ASB's, and their interactions, as observed in experiments, (see e.g. Areias and Belytschko, 2007; Rabczuk and Samaneigo, 2008).

Examining 1D modeling of shear bands, Grady (1982), Wright and Okendon (1996) and Molinari (1997) performed a perturbation analysis for the shear instability, using constitutive equations which incorporate strain and/or strain rate hardening and thermal softening. This approach ties the mathematics of perturbations with the physical material instability phenomena, suggesting that shear bands evolve at a spacing which is determined by minimum energy considerations, matching a dominant wave number, issued from the perturbation calculation. Grady (1982) accounted for a viscous constitutive equation and linear thermal softening. Later works by Wright and Okendon (1996) and by Molinari (1997) addressed this issue with a similar approach, by extending the material's constitutive law to include rate dependency (Wright and Okendon, 1996), and strain hardening (Molinari, 1997). The outcome of these works consists of analytical expressions for the spacing between shear bands. The ability of these models to predict shear band spacing was examined experimentally in several works with dynamically collapsed thick walled cylinders. Xue et al. (2004) found a good agreement for 304L stainless steel. On the other hand, significant discrepancies between the experimental results and the models' predictions were found for CP-Titanium and Ti-6Al-4V (Xue et al., 2002). Recently, Lovinger et al. (2015) found significant discrepancies between predictions from these models and their results from electro-magnetically (EM) driven TWC tests for seven different materials. It was suggested that the limited ability of these analytical 1D models, to predict the measured spacing, seems to coincide with earlier work in the literature (e.g. Rittel et al., 2006, 2008; Osovski et al., 2012), indicating that thermal softening is not the dominant factor responsible for the onset of localization.

Daridon et al. (2004) examined shear band spacing for more complex constitutive models. Using a 1D perturbation model with periodic boundary conditions, they studied the spacing between shear bands in Titanium and HY100 steel. Three material models were examined: Johnson and Cook (1983) (JC) model, a power law model and the MTS (Mechanical Threshold) model (Follansbee and Kocks, 1988). The results were compared with the experimental TWC spacing results for Titanium (Xue et al., 2002), showing that while the JC model predicted much larger spacings (by an order of magnitude), the MTS model predicted the experimental results quite well. The work of Daridon et al. (2004) follows an approach which addresses the initiation of shear bands through the *flow stress* ("strength") model, unlike other works, as shown in what follows, which search to define a *failure* or *damage* model.

Medyanik et al. (2007) defined a new criterion for shear band formation, based on experimental observations of dynamic recrystallization (DRX) in the shear bands. The onset of localization is

associated with a critical temperature for recrystallization which is of the order of $0.4\text{--}0.5 T_m$ (melting temperature) of the material. The authors presented simulations using two constitutive models: one for the bulk material and one to describe the material inside the shear band. The shear band criterion signals the shift from one model to the other and it is based on a critical DRX temperature with strain rate dependency. The JC constitutive model was used in the simulations for the bulk material, and a viscous fluid model for the material inside the shear band. The simulations agree well with the band width, their velocity and the measured temperature rise in the bands (Medyanik et al., 2007). Though good agreement was achieved, the model is restricted to a predefined perturbation as determined by a notch and the forced localization. Additional questions arise regarding the physical meaning of two distinct criteria, before and after ASB formation, and the fact that it was shown that DRX is not linked to a specific temperature rise (Rittel et al., 2008).

Considering now 2D and 3D numerical simulations which take into account also the spatial behavior of the multiple shear bands during their evolution, Areias and Belytschko (2007) suggested a two-scale model to simulate ASB's using the extended Finite Element (FE) method (XFEM). The shear bands are accounted for by using a local partition of unity. When material instability is detected, the FE temperature and displacement fields are enriched with a fine scale function which is able to model the high gradients within the shear band. They implemented this model to reproduce a large variety of shear band experiments and satisfactory agreements were achieved for many of them. For the TWC experiment, the model demonstrates the formation of multiple ASB's, yet it only shows qualitative resemblance to experimental results.

Rabczuk and Samaneigo (2008) modeled 3D shear band evolution in TWC experiments. They treat the shear bands as discontinuities, neglecting their width. The localization criterion is defined by the material instability, shifting at this point to a non-continuous space, while the discontinuity is modeled and controlled by a cohesive law. The 3D TWC simulations show the formation of multiple adiabatic shear bands only in a qualitative manner. These 2D and 3D numerical works (Firstenberg et al., 2006; Lovinger and Partom, 2009) account for the discontinuity of the shear bands' space, but they lack a physical model for shear band evolution and do not describe well the physics of the multiple shear bands' formation.

Firstenberg et al. (2006) used a different failure approach to account for shear band formation. The model defines a strain-based damage parameter, $0 \leq D \leq 1$, which evolves through the following relations:

$$D = \frac{\varepsilon_p^{eff} - \varepsilon_i}{\varepsilon_f - \varepsilon_i} \quad \varepsilon_i < \varepsilon_p^{eff} < \varepsilon_f \quad (1)$$

where ε_p^{eff} is the effective plastic strain, ε_i is the initial plastic strain, at which localization begins, ε_f is the final plastic strain, at which the stress decreases to zero. The damage parameter (D) is used to account for the decrease in the flow stress (Y) through:

$$Y = Y_0 \cdot (1 - D) = Y_0 \frac{\varepsilon_f - \varepsilon_p^{eff}}{\varepsilon_f - \varepsilon_i} \quad (2)$$

The flow stress decrease provides the positive feedback needed to cause shear localization. In Firstenberg et al. (2006), the model was used to simulate perforation tests, showing good agreement with the experimental results and reproducing failure characteristics. The damage mechanism effectively corresponds to the thermal/microstructure softening. Lovinger and Partom (2009) used this model in 2D numerical simulations to simulate multiple adiabatic shear bands and obtained a fair comparison with explosively driven TWC test results. This model was further examined

by Lovinger et al. (2011) to reproduce experimental results of EM driven (electromagnetically collapsed) TWC made of 304L stainless steel. An empirical cumulative distribution function (ECDF) was used as a quantitative measure to compare the shear band distribution in the simulations with the experiments. The simulations of the collapsing cylinder showed good agreement with the experimental results for both global behaviour and shear band distribution. However, the failure criterion used in these works is phenomenological and not physically based, thus no extrapolation from one material to the other could be done.

Numerical simulations of multiple shear bands in TWCs were also reported by Yang et al. (2008), (2009), using a mechanical-thermal coupling module available on ANSYS/LS-DYNA software. The numerical simulations demonstrate satisfactory results as far as the global behavior of shear band evolution and mutual interactions between shear bands are concerned. Yet, no quantitative comparison with the experimental results was presented for spacing or shear band distribution. Yang et al. (2008) used the JC constitutive equation that incorporates strain, strain rate hardening and thermal softening. It is not clear how localization was obtained, because material softening at the initial stage was not intense enough using the bulk softening properties. This issue was examined in the past in our numerical simulations, showing that the bulk thermal softening decreases the strength only very slightly, while significant softening is needed to reach localization. Yang et al. (2009) also examined the influence of precipitated particles or inclusions on the shear band distribution. They showed that adding heterogeneities to the model can change the directionality of the shear bands, e.g. causing all shear bands to evolve mainly in one direction (clockwise or counter-clockwise) rather than evolving equally in both directions.

Following the work of Rittel et al. (2006), who proposed a new criterion based on part of the total strain energy density, a numerical implementation of the strain energy density as a failure criterion was carried out by Dolinski et al. (2010) and by Noam et al. (2014). With this model, the two works resulted in very good agreement between the 2D simulations and test results of impacted laboratory specimens, explosively loaded plates and ballistic perforation, all involving ASB-related failure. The failure criterion which was based on experimental observations was justified analytically in the recent work of Dolinski et al. (2015).

Following the successful ability of this physically-based criterion to reproduce ASBs in forced shear scenarios (Dolinski et al., 2010, 2015; Noam et al., 2014), we pursued its application to model the formation and evolution of spontaneous multiple ASBs in collapsing thick-walled cylinders. This benchmark problem can be considered as highly challenging and discriminating, when compared to the analysis of a single shear band evolving in a solid. The experimental results reported by Lovinger et al. (2015) for several materials were available to test the performance of the numerical simulations.

The experimental work in Lovinger et al. (2015) involved the collapse of thick walled cylinders using a pulsed current generator (PCG) to create the electro-magnetic driving forces. The TWC in these tests come to a stop at the end of the test and the shear band distribution is extracted by post mortem analysis of the sectioned specimen. The specimen design enables to stop the TWC at different stages of collapse, thus allowing for examination of the shear band distribution, at different stages of its evolution.

In this work, we present 2D numerical simulations of collapsing thick walled cylinders, using the strain energy density criterion. We first present a detailed study of a typical collapsing cylinder. In the case study, we follow the evolution of shear bands by examining the evolution in time of the different thermodynamic variables. This enables extended comprehension of the complex phenomena, matching much of the physics observed in tests. We further study

different numerical and material sensitivities of the model to assess the reliability of the results. Finally, with the model calibrated for four different materials, we present a satisfactory quantitative comparison for the number of shear bands, drawing conclusions on what presumably controls the number of shear bands and their spacing, in collapsing thick-walled cylinders.

2. Numerical modeling

2.1. The numerical model

For the simulations carried-out in this work, we used a home-made 2D Lagrangian hydrocode which follows a finite difference explicit scheme. J_2 -plasticity is implemented in Wilkins' radial-return method, assuming isotropic material hardening (Wilkins, 1964). Large strain formulation is adopted throughout this work. Simulation results using this code were presented in previous works (Firstenberg et al., 2006; Lovinger and Partom, 2009; Lovinger et al., 2011).

The model uses slab symmetry (with plain strain conditions) and consists of three sandwiched cylinders, copper-specimen-copper. A boundary pressure, exerted on the external copper cylinder represents the driving force. A typical measured current signal and the calculated pressure (P) from the current density (J in Fig. 1b) are shown in Fig. 1. For sensitivity checks of the model, detailed further in this work, we used a simplified boundary condition of a half sine wave (in time), with a peak pressure of 25 kbar and duration of 2.2 μ s. The model configuration and boundary conditions are shown in Fig. 1.

For all the simulated materials, we used a Mie–Grüneisen Equation-of-state (EOS), with the linear Hugoniot relation. The strength of the intact material was represented either by Johnson and Cook (1983) (JC) model or by a Steinberg–Cochran–Guinan (SCG) model (Steinberg et al., 1980). The material parameters are listed in Table 1, and they refer to the actual material properties used in our tests (Lovinger et al., 2015).

The Johnson–Cook (JC) model which incorporates terms of strain hardening, strain rate hardening and thermal softening is defined as:

$$Y = (A + B\epsilon_p^n) \cdot (1 + C \ln \frac{\dot{\epsilon}_p}{\dot{\epsilon}_0}) \cdot (1 - (\frac{T - T_0}{T - T_m})^m) \quad (3)$$

where A , B , n , m and C are the material parameters, $\dot{\epsilon}_0$ is a reference strain-rate, taken to be $\dot{\epsilon}_0 = 1 \text{ s}^{-1}$, T_0 is the initial temperature (room temperature in this case) and T_m the melting temperature. The shear modulus, G , used with this model is constant (see Table 1).

The Steinberg–Cochran–Guinan (SCG) model incorporates terms of strain hardening, pressure hardening and thermal softening and is defined by:

$$Y = Y_0(1 + \beta(\epsilon + \epsilon_i))^n(1 + A_{SCG}P/\eta^{1/3} - B_{SCG}(T - 300)) \quad (4)$$

where A_{SCG} , B_{SCG} , n , and β are the material parameters, ϵ_i is the pre-strain, η is the compressibility defined as $(1 - \rho/\rho_0)$, P in the pressure [GPa] and T is the temperature [K°]. For this model, The elastic shear modulus is a function $G(P, T)$:

$$G = G_0(1 + A_{SCG}P/\eta^{1/3} - B_{SCG}(T - 300)) \quad (5)$$

where A_{SCG} , B_{SCG} , are the same as in Eq. (2), and G_0 is the shear modulus at room temperature and atmospheric pressure.

2.2. The failure damage model to describe shear band evolution

We use a shear failure damage model based on a strain energy density criterion. The model, incorporating a positive feedback mechanism, effectively corresponds to the thermal/microstructure

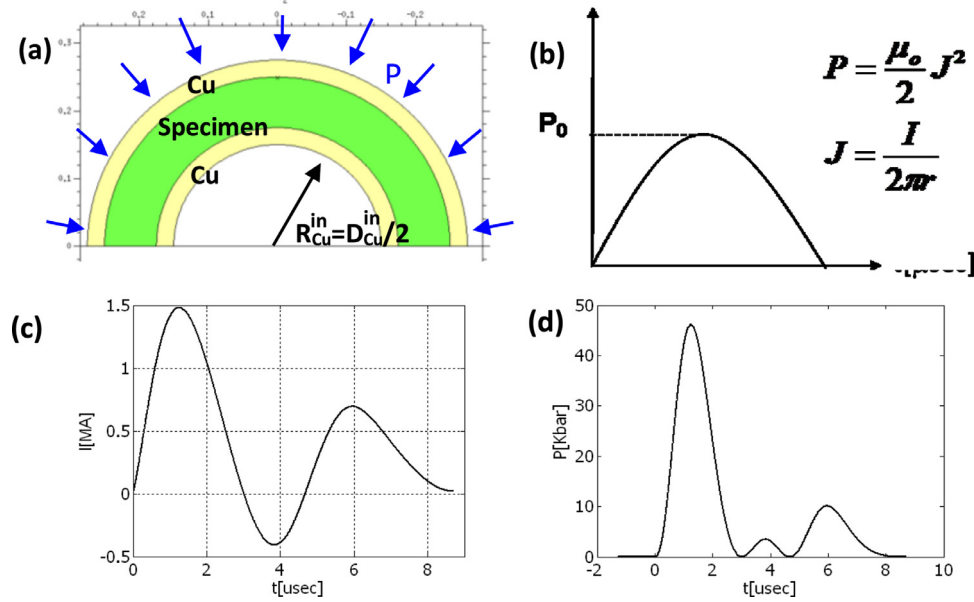


Fig. 1. The numerical model: (a) model configuration, (b) generic load-history, (c) measured current-flow in one of the EM-TWC tests and (d) the calculated magnetic pressure from the current-flow history.

Table 1
Material properties and model parameters.

JC model	ρ_0 [gr/cc]	C_0 [km/s]	S	Γ	G [GPa]	A [GPa]	B [GPa]	C	N	m	T_m [K°]
Ss304L	7.90	4.57	1.48	1.75	71.5	0.1	1.072	0.05	0.34	1.0	1356
Cu*	8.92	3.93	1.51	1.98	44.0	0.09	0.292	0.025	0.31	1.09	
SCG model	ρ_0 [gr/cc]	C_0 [km/s]	S	Γ	G_0 [GPa]	A_{SCG} [1/GPa]	B_{SCG} [1/K°]	β	n	Y_0 [GPa]	$Y_{max}^{(*)}$ [GPa]
CP-Ti	4.52	4.59	1.26	1.52	43.4	1.15	6.22e-2	210	0.1	0.85	1.45
Ti6Al4V	4.42	5.13	1.26	1.52	41.9	1.15	6.44e-2	12	0.1	1.33	2.12
MgAM50	1.78	4.50	1.26	1.52	16.5	10.3	5.09e-2	1100	0.12	0.19	0.48
Al-A356	1.66	5.14	1.69	2.38	70.0	EPP model: $Y = 0.3$ GPa					

** C_0 , S and Γ are the Mie-Grüneisen EOS parameters.

* Cu refers both to the copper specimens and to the inner and outer copper cylinders used in all tests.

(*) Y_{max} is an upper limit of the strain hardening contribution of the model: $Y_0(1 + \beta(\epsilon + \epsilon_i))^n < Y_{max}$.

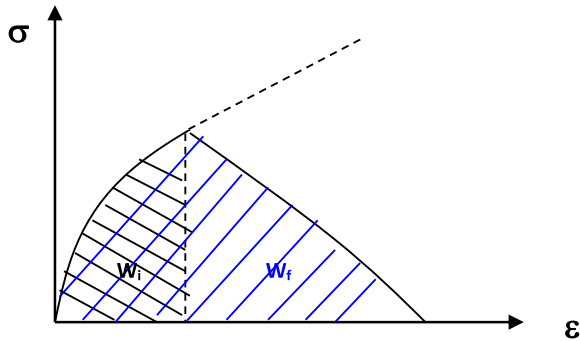


Fig. 2. Constitutive model to describe shear localization: damage model based on strain energy density criterion. The dotted line represents the strength model behavior without the damage model.

softening, which is essential to model the formation of shear localization. We refer to W , the specific plastic strain energy density, as:

$$W = \frac{1}{\rho} \int \sigma_{ij} d\epsilon_{ij}^p \quad (6)$$

where σ_{ij} are the stress tensor components, ϵ_{ij}^p are the plastic strain components and ρ is the material density.

We then define two parameters, W_i and W_f , which are graphically described in Fig. 2. W_i is the specific plastic strain energy

density until the onset of shear initiation and W_f is the plastic strain energy density at full localization when the flow stress in the band decreases to zero.

We define a damage parameter $0 \leq D \leq 1$ evolving by:

$$D = \frac{W - W_i}{W_f - W_i} \quad W_i < W < W_f \quad (7)$$

D is used to decrease the flow stress (Y) through:

$$Y = Y_0 \cdot (1 - D) = Y_0 \frac{W_f - W}{W_f - W_i} \quad (8)$$

Eq. (8) provides the positive feedback needed to cause shear localization. As W increases (with the growth of plastic strains), the flow stress decreases, softening the material and promoting additional plastic strains, and so on. The material behavior is described schematically in terms of a stress-strain curve in Fig. 2. Note that the energy criterion incorporates the physics of a process leading to shear band initiation and evolution rather than a threshold criterion such as a critical strain criterion.

3. Results

3.1. Case study – modeling the evolution of multiple ASB in a collapsing TWC

We present here a case study in which we examine the development of different thermodynamic variables such as pressure,

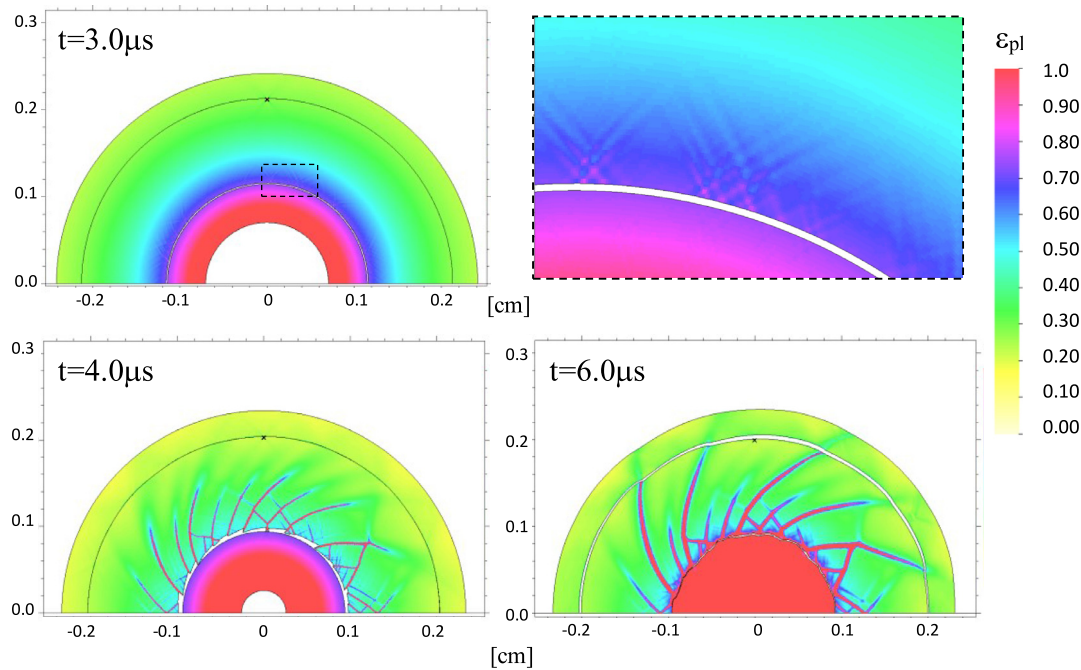


Fig. 3. Shear band evolution: maps of effective plastic strains.

plastic strain, strain rate and velocity at different stages of evolution. This case demonstrates the strength of the numerical tool in understanding the complex phenomena involved in this dynamic localization problem.

We consider a 304L thick walled stainless steel cylinder, with an outer diameter of 5.0 mm and an inner diameter of 3.5 mm. The cylinder is sandwiched between 2 copper cylinders (outer diameter 5.5 mm and inner copper diameter is 3.25 mm, respectively) and the outer boundary of the external copper is subjected to a boundary pressure of a half sine (shown in Fig. 1b) with a peak pressure of 25 kbars and duration of 2.2 μ s.

The mesh is an unstructured mesh, introducing a spatial numerical perturbation to break the symmetry of this one-dimensional problem. The initial perturbation will be discussed further in detail, and will be shown that it does not influence the characteristics of the shear bands distribution.

3.1.1. Effective plastic strains

Fig. 3 shows maps of effective plastic strains. The time duration for the collapse of the cylinder until it comes to a full stop is about 6 μ s. The plastic strains at the inner boundary are the highest, and at $t = 3.0 \mu$ s, when they reach the value of ~ 0.45 , fluctuations in the plastic strain are evident (see zoomed frame in Fig. 3).

Fig. 3 shows at $t = 3.0 \mu$ s 2D fluctuations in the plastic strain field with a general pattern of lines at $\pm 45^\circ$ with points on the boundary with slightly higher plastic strains. These points serve as “embryos” from which shear bands can evolve. The competitive evolution is captured, as some of the shear bands propagate to longer distances, and the neighboring shear bands come to earlier stop and travel shorter distances. Upon propagation of the shear bands, the stress is released in their vicinity, as strength is decreasing on the sheared surfaces, by release waves emanating from them. This “shielding” effect as referred to in Xue et al. (2004) will be further demonstrated, in Section 3.2.2.

3.1.2. Pressures

The boundary pressure is exerted on the external boundary of the outer copper and propagates in the radial direction. Radial re-

verberations of the waves accelerate the cylinders while the inner copper cylinder, due to the mechanical impedance mismatch, is accelerated faster. Thus, during the collapse, the inner boundary of the ss304L specimen is not in contact with the copper, creating a free surface. At $t \sim 4.4 \mu$ s the inner copper collapses to the center, creating a strong outgoing shock wave. At $t = 4.6 \mu$ s the shock wave which emanated from the center reaches the free surface of the inner copper, and a release wave returns to the center, creating tension, and its external surface starts moving outwards. At $t = 4.8 \mu$ s the ss304L inner boundary and the copper impact each other, creating pressures of the order of 5 GPa. Finally, at $t = 6 \mu$ s, pressures are already of the order of the material strength and no additional propagation occurs.

3.1.3. Velocities

The radial velocities of the specimen during the collapse are ~ 200 m/s. The radial velocity matches that of the explosively driven TWC experiments (Xue et al., 2004), yet in those experiments the time of collapse is about 25 μ s as compared to 6 μ s in our tests. This difference matches the geometry-scale of ~ 4 , between the two sets of tests. The inner copper is moving with a higher velocity (400–700 m/s), detaching from the specimen boundary, creating a gap between the specimen and the inner copper (with free surfaces). This gap is maintained for the most part of the collapse.

The inward velocity is decreasing gradually, due to dissipation of energy by plastic work of the specimen itself. Before coming to a stop on the inner copper cylinder, these velocities slow down to ~ 50 m/s.

When shear bands evolve, we notice higher velocities of the bulk material which is “trapped” between shear bands. This relative velocity is what causes the “jigsaw” displacements, noticeable in all of the experiments (for each of the materials), see the zoomed figure at time 4.0 μ s. An example of this is shown in Fig. 4, demonstrating this phenomenon in a Ti6Al4V collapsed specimen, as reported in Lovinger et al. (2015). At later times the velocity vector changes direction as the shock wave emanating from the center, propagates outwards, resulting in outward radial velocities.

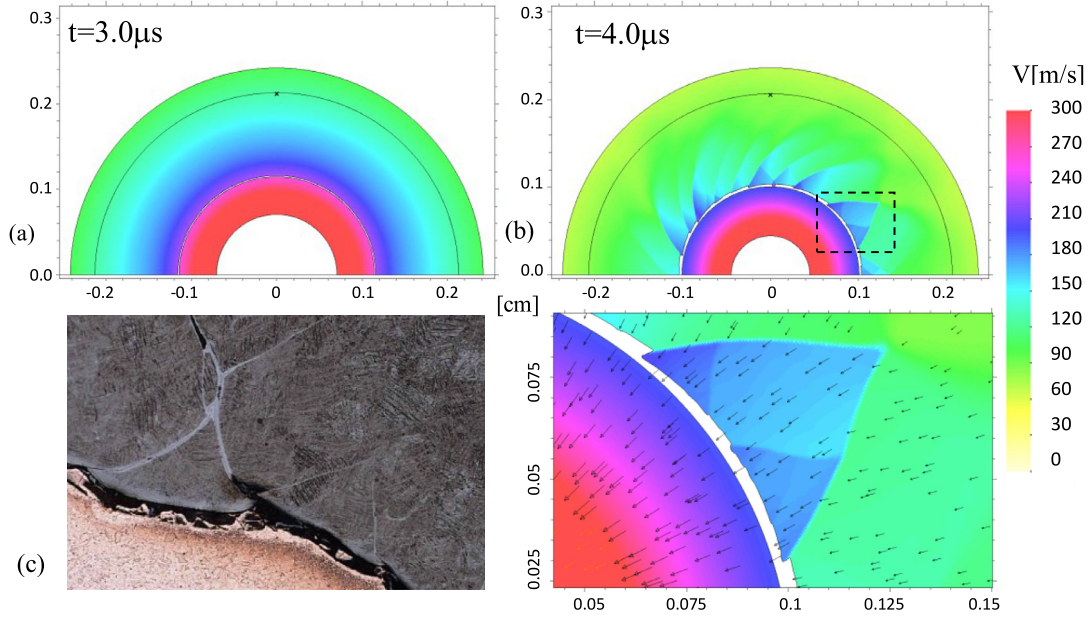


Fig. 4. Velocity maps: (a) at $t=3\ \mu\text{s}$, (b) at $t=4\ \mu\text{s}$ (with zoomed area) and (c) experimental result for Ti6Al4V (from Lovinger et al. (2015)).

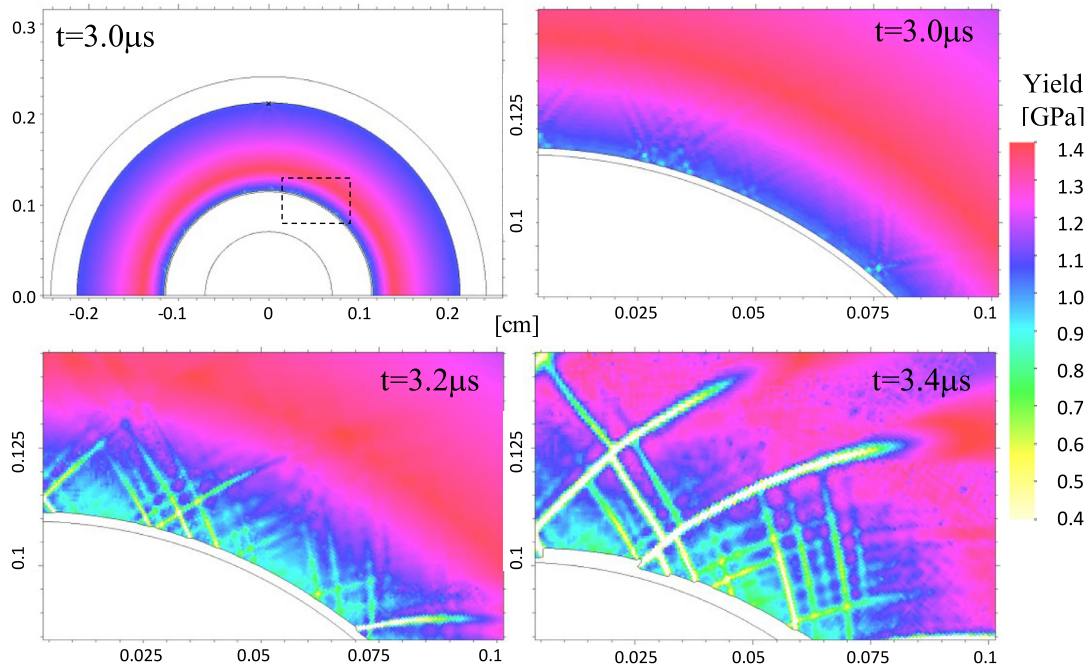


Fig. 5. Shear band evolution: flow stress maps at different stages of shear band evolution.

3.1.4. Strain-rates

The strain rate at the inner boundary of the specimen, upon initiation is $2\text{--}3 \cdot 10^5\ \text{s}^{-1}$, while within the shear bands, the strain rate reaches values of $3\text{--}4 \cdot 10^6\ \text{s}^{-1}$ during band evolution. The strain rate relaxes as the specimen comes to a stop at $t \sim 6\ \mu\text{s}$.

3.1.5. Flow stress (strength) maps

The maps of the flow stress (strength) provide additional insight into the evolution of shear bands, as the stress decreases gradually in the evolving shear bands and reduces to zero when a calculated cell reaches full shear (when W reaches W_f , see Eq. (8)). Fig. 5 shows the stages of initiation, growth and interaction between shear bands. The fluctuations in the flow stress field ob-

served at time $3.5\ \mu\text{s}$ develop for some into actual initiations. The two earlier initiated shear bands seen on the left hand side of the zoomed figure cause a “shielded” area, deactivating the potential initiation sites between them. The competitive growth of the shear bands is demonstrated in a comprehensive manner, following gradually the stages of propagation.

When two developed shear bands meet, the bulk material which is trapped between them moves inwards (having a radial relative velocity, as shown above) causing the jigsaw structure at the inner boundary. At $t=4.8\ \mu\text{s}$ the inner copper impacts the specimen, “smoothing-out” this disturbed boundary. The broadening of shear bands, seen at later stages, seems to be a result of weak radial tensile forces. The tensile opening of shear bands is evident

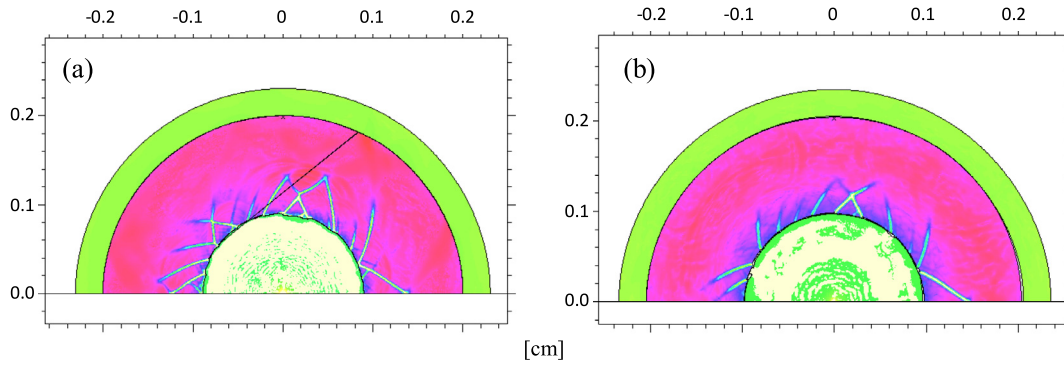


Fig. 6. Final stage of collapse (yield maps) with different boundary pressure impulses: (a) 25 kbar per 2 μ s and (b) 50 kbar per 1 μ s.

through pore growth and coalescence in post mortem fractography of the specimens, as shown in Lovinger et al. (2015).

3.2. Sensitivity checks

In order to establish the credibility of the numerical modeling, and its ability to be compared with experimental results, we conducted sensitivity checks for the load (the boundary pressure exerted on the external copper) and for the initial perturbations in the simulations. Later on we shall discuss the influence of the mesh size on our results.

3.2.1. Boundary pressure sensitivity study

The main purpose of this part of the study was to explore how sensitive the spatial distribution of shear bands is to the exact load, and if we can pursue a quantitative comparison to experimental results, given the accuracy of our current-flow measurements. In Lovinger et al. (2011), we examined the influence of the peak pressure value and showed that a change of 20% in the pressure, for which we achieved good agreement with the experimental spatial SB distribution, is very significant. We used in Lovinger et al. (2011) a half sine load with duration of 2.2 μ s (see Fig. 1b) and varied the peak pressure. The numerical simulations showed no evolution of shear bands with the low boundary pressure, and a full breakup of the specimen for the high boundary pressure. We concluded that we can accurately determine the peak pressure value by calibrating it such as to achieve the final geometry of the specimen, as measured after it is recovered. To further examine this conclusion, we conducted simulations with two loading cases, maintaining the same impulse: A peak pressure of 25 kbars for 2 μ s and a peak pressure of 50 kbar for 1 μ s. The shear band distributions, shown in Fig. 6, seem to be practically identical for the two cases. This result strongly suggests that the exact pressure history has a weak significance on the spatial distribution of shear bands, and that the total impulse driving the specimen is the main factor dominating the shear band distribution. This conclusion is very significant, since it relaxes the demands on accurate current measurements, which are difficult to perform in high pulsed power machines. Thus, we do not have to determine the exact boundary pressure in each test. Practically, we could use a single sine wave rather than input the entire oscillating signal and calibrate it to achieve the final geometry of the specimen.

Moreover, we expect the simplified representation of the boundary pressure to differ, to some extent, from the actual boundary conditions of the magnetic field, as we are not using coupled magnetic-hydrodynamic (MHD) calculations. Triantafyllidis and Waldenmyer (2004) discusses the limitations of calculating electro-magnetic forming problems with a magnetic boundary pressure in comparison to full MHD calculations. A 10–15% dif-

ference in results was reported in Triantafyllidis and Waldenmyer (2004) between the two approaches. These results point out that an equivalent boundary pressure could be a relatively good estimation, and it could be further modified to compensate for some of the missing magneto-thermo-mechanical coupling at this stage.

3.2.2. Initial perturbations

The plane-strain geometry of a collapsing cylinder loaded by a spatially-uniform boundary condition is in fact a 1D problem. To achieve shear band initiation, some perturbation is needed to break the 1D symmetry. The initiation of shear bands is achieved in the simulations by numerical perturbations of the unstructured mesh we are using. In order to confirm that the initial perturbations do not influence the shear band distribution in any way, we examined systematically the influence of these initial perturbations.

Fig. 7 shows a comparison of two calculations which differ only in their mesh structure: Fig. 7a shows the result using a structured polar mesh with uniform “rays of cells” and Fig. 7b shows the result using the unstructured mesh. The latter is able to adjust to the occurrence of large changes in the geometry (large deformations and strains) which occurs at late stages of shear band evolution with large plastic strains, for which we use remeshing. The use of geometrical erosion (deleting cells which reach a geometrical threshold) is possible at this stage but we found it as a numerical step which intervenes with the physics of the shear bands' evolution. When using erosion, the numerically deleted cells, create new free surfaces, resulting with rarefaction waves emanating from them. It can be seen that when we use a perfectly polar structured mesh, no shear bands initiate and we reach a perfect 1D behavior. With the unstructured mesh, the symmetry breaks and with perturbed fields of strain, velocity and pressure, initiation occurs at the inner boundary.

The main issue we wanted to explore was whether the shear band distribution and spacing are influenced by the pattern of the unstructured mesh. To examine this point, we used the model with the structured mesh and applied perturbations of different amplitudes and wavelengths. The perturbations consisted of small geometrical changes of the inner radius of the specimen, defined by:

$$R = R_0 + A_0 \cos\left(\frac{\pi}{2} \cdot n \cdot t\right) \quad (9)$$

where A_0 is the amplitude of the perturbation, n is the number of waves on the perimeter and t is an angle vector along the perimeter. Fig. 8 shows three cases we examined with different number of waves: 10, 100 and 200. The amplitude A_0 was determined at first to be of the order of the microstructure, setting $A_0 = 1 \mu\text{m}$. Using such amplitude caused a shear band to initiate at the peak of each wave. As the unstructured mesh perturbation is a numerical one, and is much smaller than the geometrical scale, we used

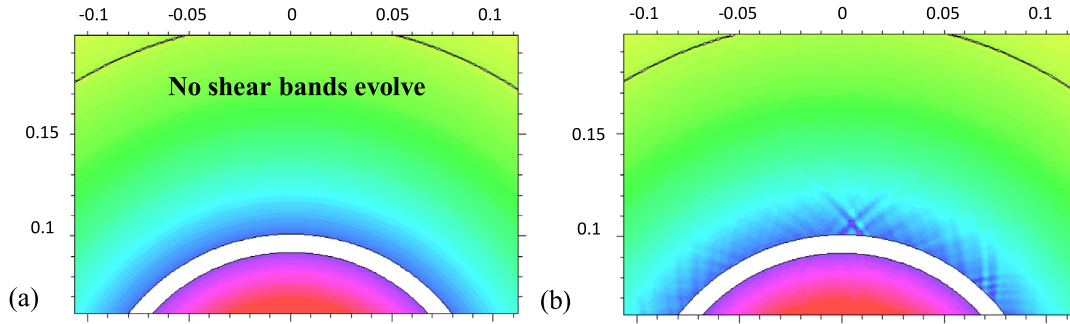


Fig. 7. The influence of mesh structure: (a) no shear banding in a perfectly structured mesh and (b) shear band initiation with an unstructured-mesh.

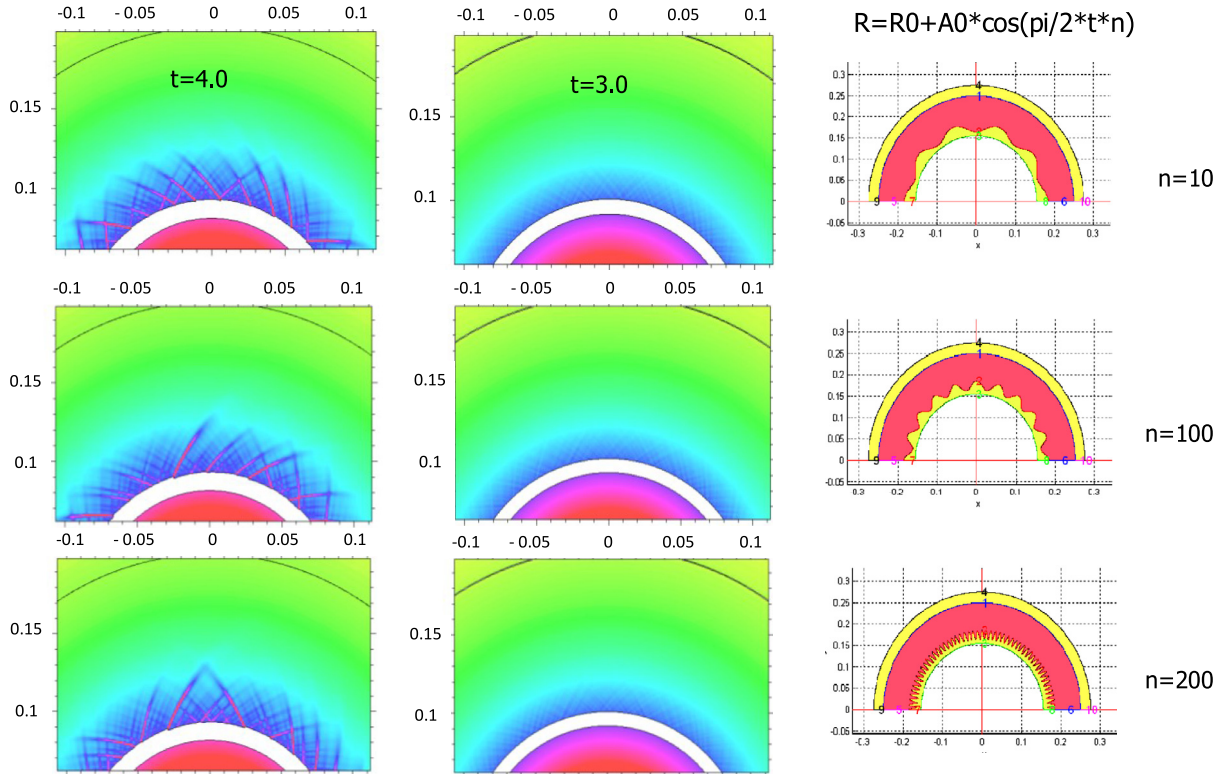


Fig. 8. The influence of initial perturbation on shear band distribution examining different wave numbers.

eventually a value of 10^{-4} μm for perturbing the radius. The perturbed radii in Fig. 10 are exaggerated just for the purpose of presentation. The shear band initiation and evolution is presented in Fig. 10 at two different times: $t=3.0\mu\text{s}$ and $t=4.0\mu\text{s}$. The shear band distributions seem very similar for all cases, yet, for quantitative comparison we sketched out the shear-bands in the simulations and used an empirical cumulative distribution function (ECDF) (Lovinger et al., 2011) to compare them. The ECDF does not follow a particular parametric form of a probability function but produces a non-parametric density estimate that adapts itself to the data. The stair-step function simply assigns a probability of $1/n$ to each of the n observations in a sample. We use Greenwood's formula (Cox and Oakes, 1984) for calculating lower and upper confidence bounds for the calculated ECDF.

The results, shown in Fig. 9, lie well within the upper and lower limits of the ECDF estimation. Taking into account the probabilistic character of the shear band formation, the ECDF comparison shows that the three results are practically similar. From these simulations, it appears that as long as the perturbation amplitude is small and of the order of a numerical perturbation (e.g. 10^{-10} m), this

pattern has no observable influence on the shear band distribution itself. On the other hand, for a large enough perturbation, the case becomes similar to that of forced nucleation of shear bands, and the latter are dominant in this specific region, as exemplified in Fig. 10.

An additional case was examined, for which we changed the properties of two single cells, using the structured mesh, with no additional perturbation. For these two cells, the first parameter of the damage model, W_i , was decreased by 33%. This can simulate for example, a mechanical or a microstructural damaged point. At these two points, shear bands evolved at an early stage, before other shear bands initiated at the inner boundary. The results, shown in Fig. 10, lead to several conclusions:

- (1) The two single-cell perturbation was enough to perturb shear bands on the entire boundary of the specimen.
- (2) The shear bands, in the zones far from the point perturbations, evolve in a similar distribution as the other cases shown above: The same shear band distribution is achieved with the sinusoidal perturbation, the single-cell perturbation or the

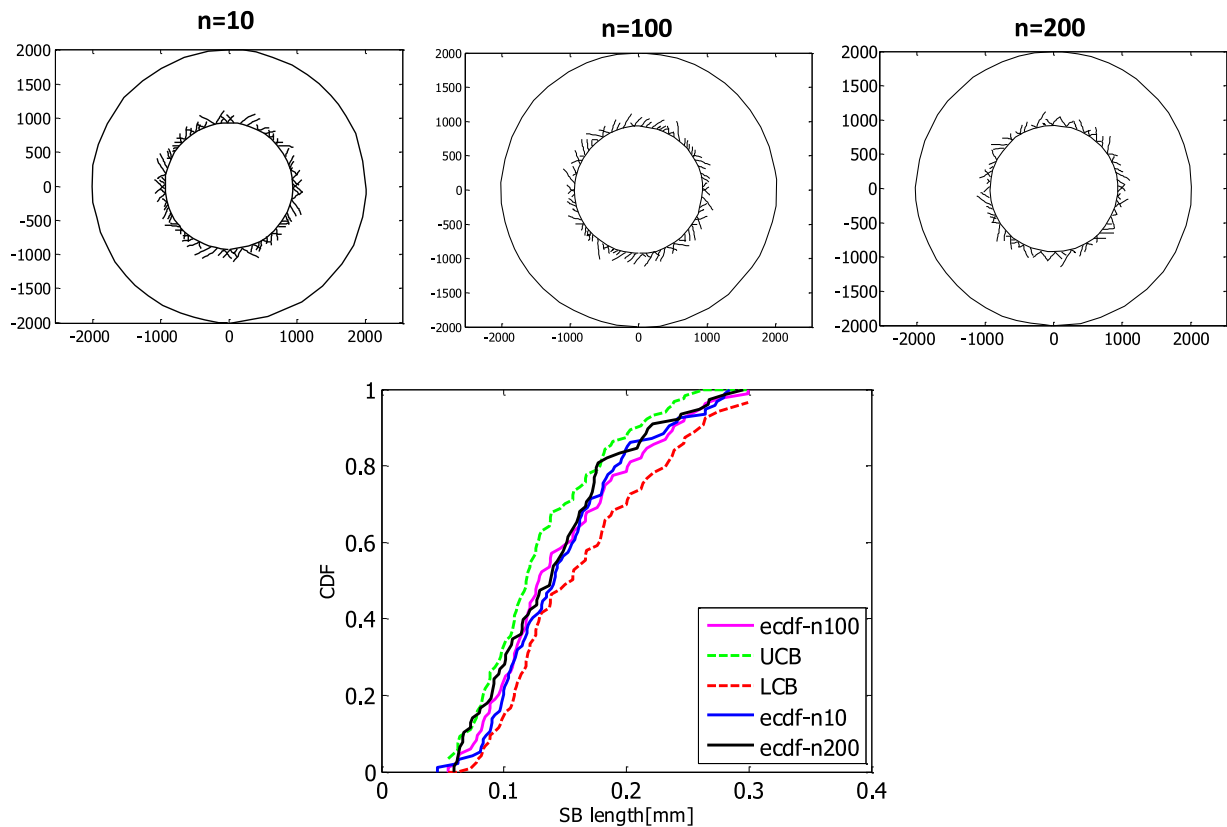


Fig. 9. Influence of initial perturbation on shear band distribution examining different wave numbers (10, 100, 200) – comparison of the ECDF, with lower (LCB) and upper (UCB) confidence boundaries.

full-space unstructured mesh perturbation. This further establishes that the shear band distribution is a result of the physics and not a result of the amplitude or character of the initial perturbation.

The much earlier propagating shear bands demonstrate very clearly the “shielding effect”. We can identify three different zones: the neighboring zones at the side of a shear band, the zone between the two shear bands, which has enhanced shielding, and the far zone which is not affected by them.

The results shown here, with single shear bands propagating much earlier, and to much longer distances than the rest of the specimen, can explain the phenomenon observed in some of the specimens. For example, in the SS304L#2 specimen (Fig. 10b), a single shear band evolved through the whole thickness, while the rest of the bands evolved to much shorter lengths. As discussed above, one can assume that this is a result of a “strong” perturbation forcing shear localization, such as a machining flaw.

3.2.3. Mesh size influence

The influence of mesh size in numerical modeling, using damage models, is always an important issue. As we use meshes with high resolutions, and a remeshing mode, one may expect the influence of mesh size to be small.

In Lovinger et al. (2011), using a comparable model to the one we are using in this work and a critical strain criterion, we presented a mesh sensitivity study of the numerical model. We found the mesh sensitivity, using the current model based on a strain energy criterion to be the same as for the strain criterion (Lovinger et al., 2011). Thus, we refer to the full comparison conducted in Lovinger et al. (2011) and state here only the main conclusions. The sensitivity check was conducted using two cell sizes, 5 μm and

10 μm and examined the influence of mesh size on the number of shear bands and on the shear band distribution.

We found that the shear band distributions for the two resolutions are close and that the number of shear bands in the two cases was the same. However, when comparing the maximum length of the shorter shear bands, namely those which come to a stop at an earlier stage of evolution, the two distributions differ. In fact, the lower resolution calculation resulted in longer short shear bands than the higher resolution ones. This result indicates that for the fine resolution, the shear band velocities remain quite the same as for the coarser resolution, yet the shielding effect is more enhanced, causing the initiated shear bands to stop at shorter lengths.

We concluded from this comparison that:

- (1) The initiation stage is not influenced significantly by the mesh size, as also shown by the same number of shear bands in the two cases.
- (2) The mutual interaction between shear bands is influenced by the mesh size, causing a higher shielding effect for the higher resolution. We believe this to be a result of the differences in remeshing in the two cases: when remeshing occurs with smaller cells, the remapping of variables at the deformed areas on the shear bands maintain closer values to the maximum values obtained in the shear bands. When the cells are coarse, the values are more averaged-out and the influence of the extreme values within the shear band travel out in a slower manner.

3.3. Numerical versus experimental results

After studying the ability of the numerical simulations to capture the evolution of multiple adiabatic shear bands and their mutual interactions, we calibrated the energy model to best-fit the

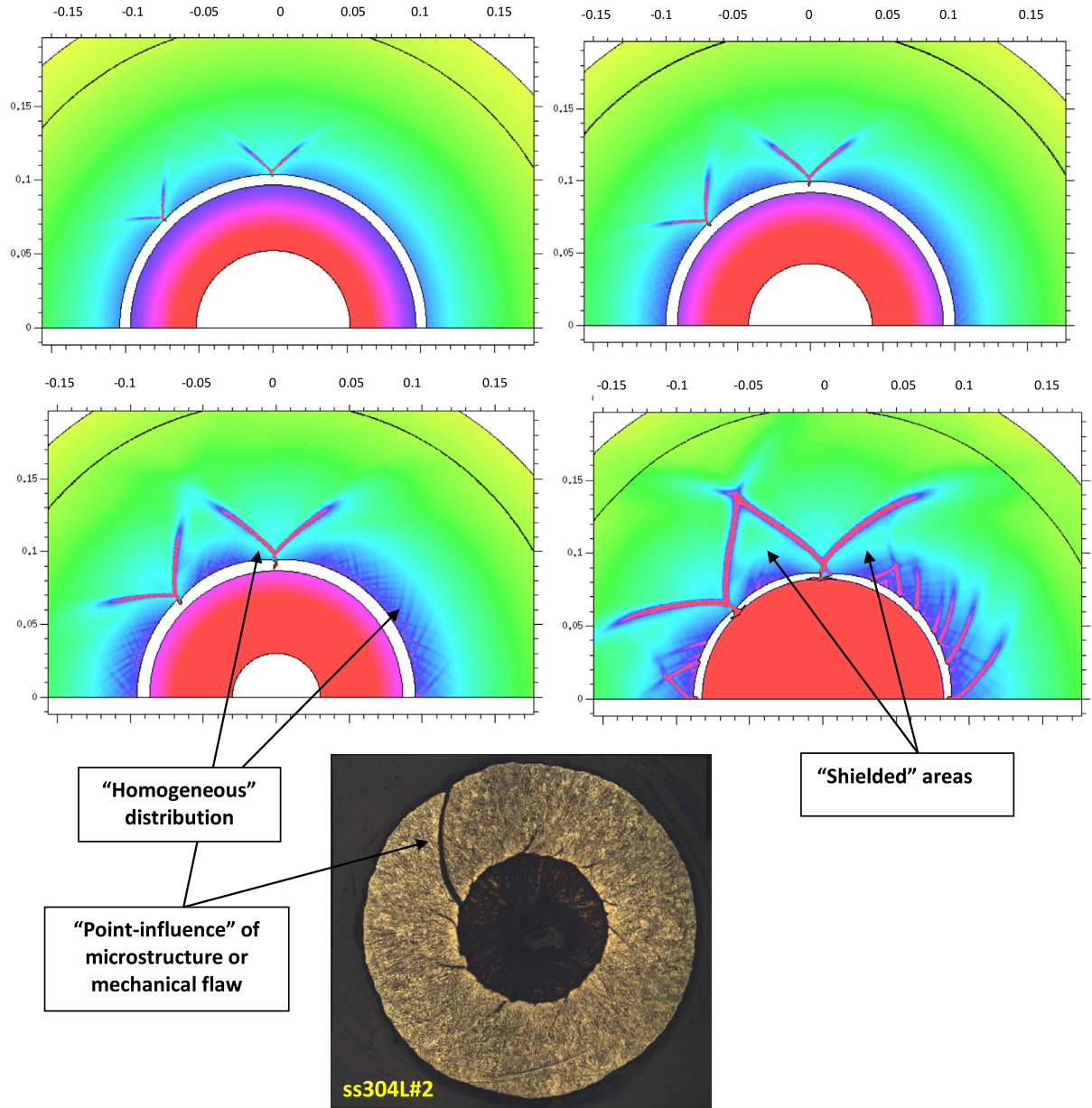


Fig. 10. Shear band evolution in a case of a structured mesh with only two “weak” cells, and a comparison with results observed for specimen SS304L#2.

experimental results for four materials: SS304L, Pure Titanium, Ti6Al4V and Mg-AM50. For this purpose, we examined how the model parameters W_i and W_f affect the shear band distribution in order to reach the best fit with the data.

3.3.1. Calibration process

Using a boundary pressure history of a half sine with a duration of $2.2 \mu\text{s}$, we calibrated the maximum pressure P_{\max} to reach the best fit for the final measured geometry (cylinders radii). In order to extract the shear band results, namely their number and lengths, we proceeded as follows: For the experimental results we sketched the specimen geometry and shear bands (as detailed in Lovinger et al., 2015, 2011) as obtained from the optical microscope pictures. For the simulation results we had to define a criterion for which a shear band is identified. A “shear-band cell” is defined after full failure, when $W = W_f$ is reached. From numerical considerations, we chose for the analysis a value close to full failure, namely a shear band is fully formed and identified when 90% of the max-

imum decrease from W_i to W_f is reached:

$$W_{SB} \text{ (criterion in simulation)} = [W_i + 0.90(W_f - W_i)]. \quad (10)$$

The simulation parameter we used to outline the shear bands was a map of strain energy density, with the above criterion as a threshold for shear band initiation existence.

3.3.2. Parametric study of w_i and w_f

The parametric study examines the influence of each of the parameters W_i and W_f on the shear band distribution. The shear band distributions for SS304L with different values of W_i and W_f are shown in Fig. 11. The distributions are shown as strength maps, tracking the paths of decreasing strength, and not only the shear band cells which reach the above threshold criterion (as we use later on in the final comparison). We found this to better illustrate the influence of the parameters. In the left hand column in Fig. 11, W_f is kept constant with different values of W_i , and in the right hand column W_i is kept constant while W_f changes.

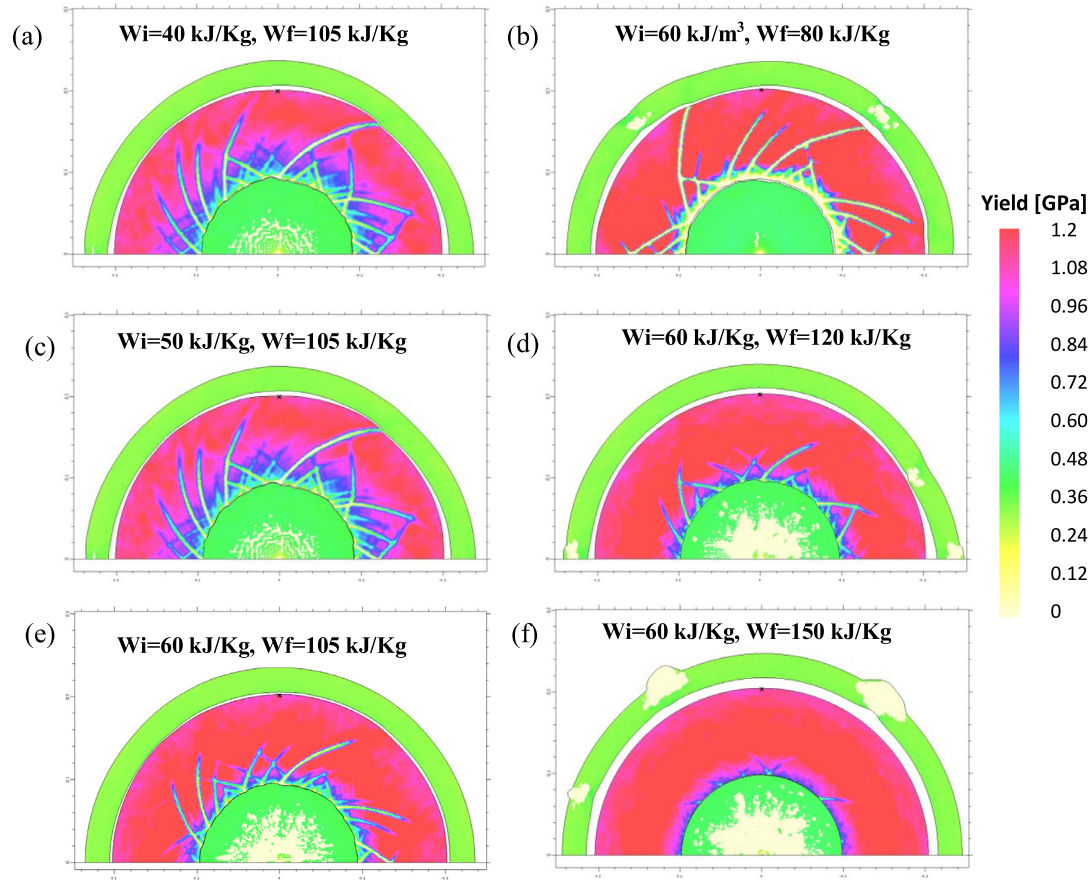


Fig. 11. Shear band distribution in SS304L for different values of W_i and W_f .

The following important conclusions can be drawn from these results:

- (1) W_i controls the length of the short shear bands
- (2) W_f controls the length of the long shear bands
- (3) The difference $W_f - W_i$ controls the homogeneity of the distribution. When the difference is small (as in Fig. 11b when $W_i = 60 \text{ kJ/kg}$, $W_f = 80 \text{ kJ/kg}$), less shear bands evolve and they are well developed. When the difference is large, the distribution is more homogeneous and more shear bands are evident. This will be further discussed in Section 4.

It can also be seen that for some of the simulations, the shear bands mostly evolve in one direction (e.g. $W_i = 50 \text{ kJ/kg}$, $W_f = 105 \text{ kJ/kg}$), and in others, shear bands evolve at both $\pm 45^\circ$ directions. This seems to be a statistical behavior, which we observed also in different experiments, and not a feature to further address here.

The shear band distribution for pure Titanium with different values of W_i and W_f is shown in Fig. 12. Following similar values as for SS304L, the shear bands evolve much too fast and the left hand column shows two results where many shear bands are evolving and breaking up the specimen, while still in the process of collapse, even before the specimen stopped its inward motion. The two results on the right hand column of Fig. 12 ((b) and (d)) show the best fit we achieved with $W_i = 150 \text{ kJ/kg}$, $W_f = 220 \text{ kJ/kg}$ and a result with higher values of W_i and W_f . The comparison with the experimental result is shown later in Fig. 14.

The shear band distributions for Ti6Al4V with different values of W_i and W_f are shown in Fig. 13. For Ti6Al4V we examined

two specimens: (1) the early stage arrested specimen for which the geometry is well defined, and which was used to calibrate the model parameters; (2) the later evolution stage when the specimen broke along the shear bands and resulted in a distorted geometry. This case was examined with a higher load, using the calibrated model parameters from the early stage specimen, to try and reconstruct the final geometry of this case as well. The difference between the two simulations was only in the boundary pressure value. For both Ti6Al4V and MgAM50 specimens which were stopped at very low final strains, the load was significantly weaker. We calibrated the peak pressure, for the simple half-sine loading to match the final geometry. We found it to be $P = 15 \text{ kbars}$, comparable to $P = 25 \text{ kbars}$ which fits the data for the CP-Ti and the SS304L specimens). The best fit for Ti6Al4V was achieved with $W_i = 70 \text{ kJ/kg}$, $W_f = 90 \text{ kJ/kg}$. To achieve the combination of a small number of shear bands and well developed ones, a small difference between W_i and W_f was needed, while W_f was chosen to fit the length of the developed shear bands in the best manner. Fig. 13b and d shows results of the best fit for W_i and W_f and of a close set of W_i and W_f which shows differences in shear band lengths, which did not fit the experimental results. For the late-stage Ti6Al4V specimen, we used the calibrated values of W_i and W_f and $P = 25 \text{ kbar}$ for pressure, since similar loading conditions as for the CP-Ti and SS304L specimens were reached.

Fig. 13a shows a stage during the collapse in which some of the shear bands propagated through the whole thickness and the fragments between the shear bands start moving as rigid bodies without additional plastic strains. These fragments are comparable to those obtained in our tests (as seen in the Fig. 13c). The

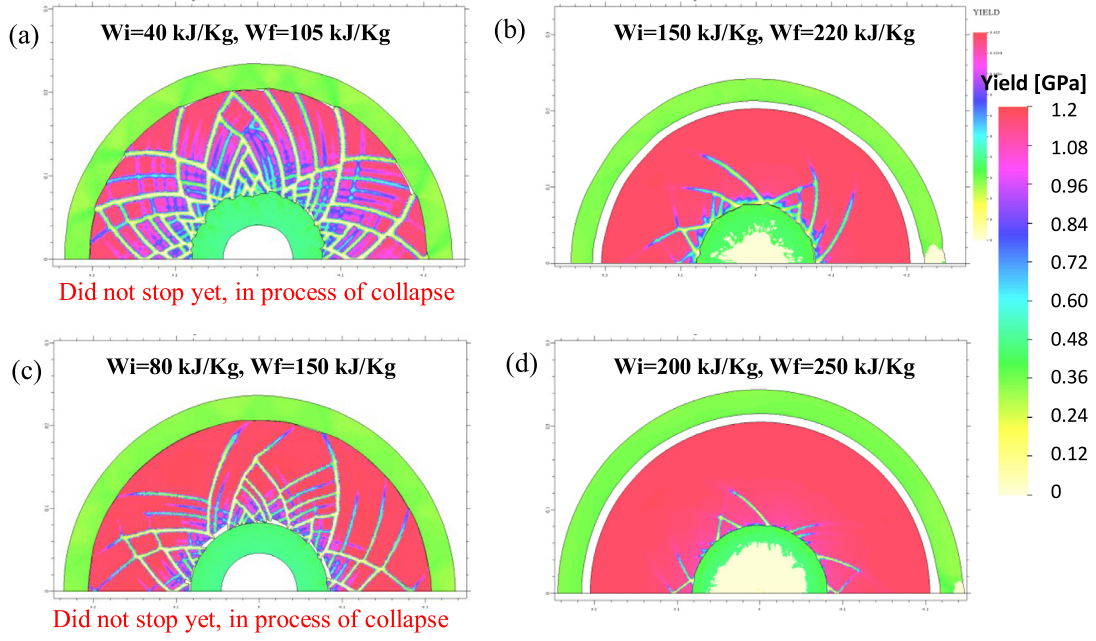


Fig. 12. Shear band distribution in pure Titanium for different values of W_i and W_f .

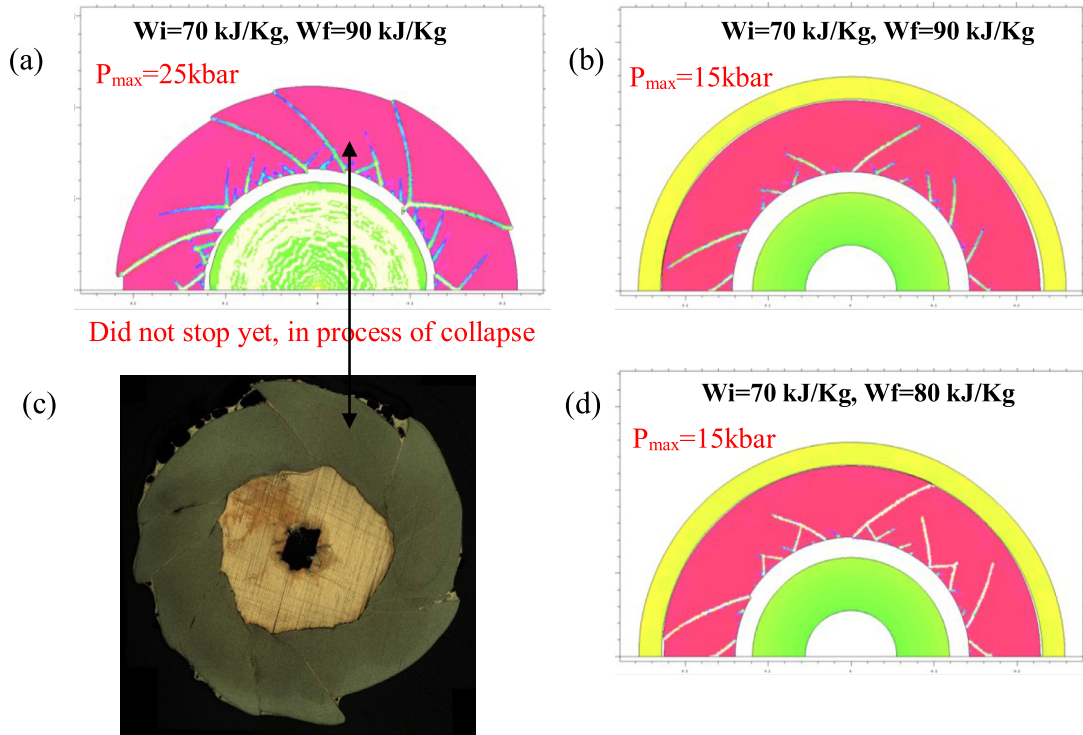


Fig. 13. Shear band distribution in Ti6Al4V for different values of W_i and W_f with a weak load ($P_{max}=15$ kbar) and a strong load ($P_{max}=25$ kbar) compared to an experimental result.

simulations were not able to reconstruct the final geometry and the experimental collapse of the fragments. We believe that the boundary conditions in the actual test change significantly when the shear bands reach the external boundary, and the magnetic pressure history no longer follows the simplified effective boundary pressure we assumed.

For the AM50 a similar parametric study was conducted and is not shown here in detail.

3.3.3. Calibrated material parameters

Fig. 14 summarizes the results of this chapter, showing the comparison between the calibrated simulations and the experimental results, for the four materials. The simulation maps in Fig. 14 show step functions of the strain energy density for each of the materials – above (light color) or under (dark color) the previously defined threshold criterion (Eq. (10)). The comparison between simulations and experimental results are shown in Table 2:

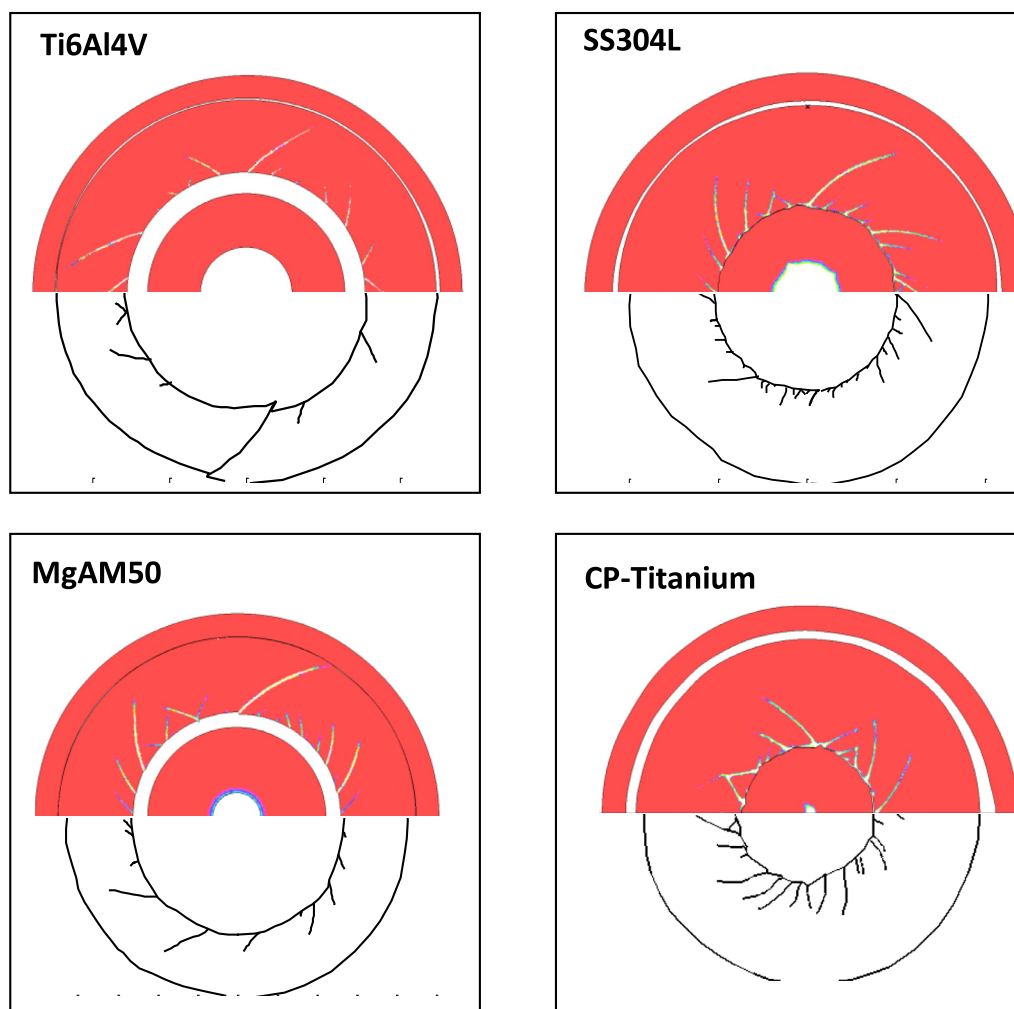


Fig. 14. Shear band distributions: comparison between calibrated simulations (upper half) and experimental results (lower half) for SS304L, CP-Ti, Ti6Al4V and MgAM50.

Table 2

The calibrated simulations results and experimental data.

	D_{in}^* final EXP [mm]	D_{in}^* final SIM [mm]	Peak pressure-on-boundary [kbar]	W_i [kJ/kg]	W_f [kJ/kg]	$(W_f - W_i)/W_i$	N_{SB} Exp	N_{SB} Sim
ss304L	1.98	1.94	25	50	105	1.1	52	48–50
MgAM50	2.44	2.54	10	60	100	0.66	35	34
CP-Ti	1.58	1.60	25	150	220	0.46	32	30–32
Ti6Al4V	2.87	2.86	15	70	90	0.28	21	22–24

* D_{in} - the final inner diameter of the specimen after collapse.

The final geometry is obtained with errors of 1–4% (which could probably be improved if the boundary pressures were altered in the parametric study with higher resolution) and the number of shear bands matches the experimental results within 5%.

$(W_f - W_i)/W_i$:

$$N_{SB} = 36 \left(\frac{W_f - W_i}{W_i} \right) + 12 = 36 \frac{W_f}{W_i} - 24 \quad (11)$$

The number of shear bands is related to the initial strain energy density which is needed to initiate a shear band, and to the ratio between W_f and W_i , referring to the amount of energy needed to obtain full localization.

We suggest that the ratio $(W_f - W_i)/W_i$ is related to plasticity micro-mechanisms, some of which delay or slow down the rate of shear band evolution. Such mechanisms could be twinning or even martensitic transformations (Rodriguez-Martinez et al., 2013). This, coincides also with the work of Osovski et al. (2012) suggesting for CP-Titanium that twinning delays strain localization. The above reasoning can be applied to the different investigated materials, as follows:

4. Analysis and discussion

4.1. The number of shear bands

Seeking to define a relation between the experimental results and the energy density values calibrated for each of the materials, we plot the number of shear bands as a function of the normalized parameter $(W_f - W_i)/W_i$, shown in Fig. 15.

An empirical linear relation was found between the number of shear bands and the non-dimensional energy parameter

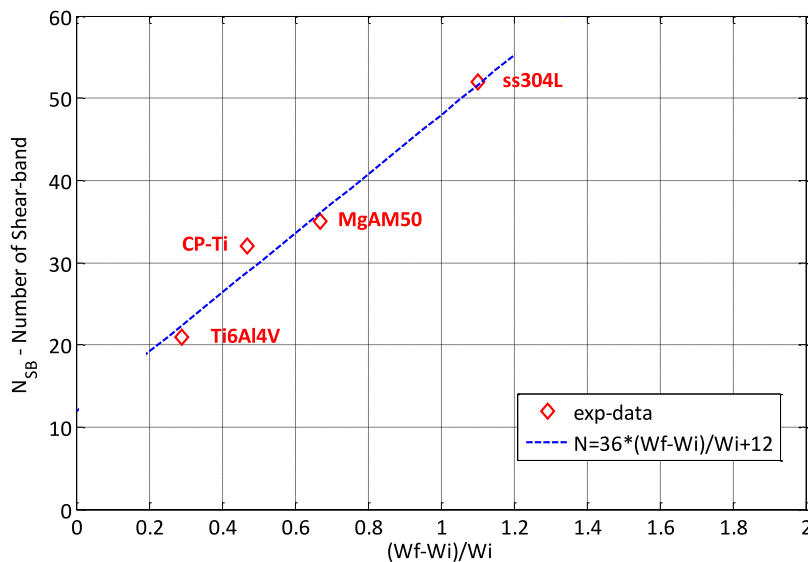


Fig. 15. The number of shear bands as a function of the normalized parameter $(W_f - W_i)/W_i$.

- *Ti6Al4V* undergoes dynamic recrystallization and no additional plasticity mechanisms are identified (minor fractions of twinning are possible only at very low temperatures or under severe plastic deformation (Coghe et al., 2012)). Consequently, localization develops rapidly.
- In *CP-Titanium*, significant twinning is evident (Mercier and Molinari, 1998), as well as in our specimens. In this case, localization is delayed as some of the strain energy is dedicated to the twinning mechanism process. During this delay, more localizations sites are able to evolve.
- In *MgAM50* twinning is evident. As for the case of pure Titanium, localization is delayed as some of the strain energy is dedicated to the twinning evolution and allowing for more localization sites to evolve.
- *SS304L* undergoes both twinning and martensitic transformation. In this case, more of the strain energy is dedicated to both processes of twinning and the martensitic transformations, now holding back for a longer period the process of localization, enabling more localization sites to be activated. Thus, *SS304L* showed the highest number of shear bands.

Given the observed linear relationship between the number of shear bands and the ratio W_f/W_i , one could expect that no shear bands would be formed when $W_f/W_i = 1$, if the trend line passes through the origin. In our simulations we find support for this claim. When we set $W_f \approx W_i$, the simulations showed a homogeneous deformation pattern and a nearly simultaneous failure on the whole inner surface, without marked shear bands. Taking into account the existence of inhomogeneities in the material properties, we may expect to find potentially at most a few localizations. It is not clear from the existing data if to expect a small but finite number of shear bands as $W_f \approx W_i$ (as we actually have in the linear fit of our results), or if it actually reaches the origin of zero shear bands with a non-linear function.

For a more general description of these results, which can be compared with data for explosively driven (ED)-TWC experiments (Xue et al., 2004, 2002; Meyers et al., 2003), we now convert the number of bands to spacing results. The definition of spacing between shear bands is explained and detailed in Lovinger et al. (2011). The spacing is referred to the specimen's geometry upon localization. Fig. 16 is a plot of the band spacing as a function of the parameter $(W_f - W_i)/W_i$ for both the explosively and electromagnetically driven tests.

An inverse relation seems to fit the results quite well. This is not surprising as the number of shear bands is linearly dependent on the ratio W_i/W_f , and the spacing is related to the inverse value of the number of shear bands. Both ED-TWC and EMD-TWC experimental results lie within a range of $\pm 20\%$.

4.2. Mechanism for shear band occurrence in TWCs

Based upon the findings from the experimental results and the results from the numerical analyses, we suggest the following three-stage mechanism for shear band evolution in collapsing thick wall cylinders:

Stage 1 – The instability stage

- At this stage, plastic flow becomes unstable prior to localization. This was demonstrated in the numerical simulations as a break in symmetry and in the inhomogeneous flow at the inner boundary of the collapsing cylinder. Within the unstable thermodynamic fields (of strain, pressure, velocities, temperature) potential initiation sites evolve with point-elevated values of strain/velocity/temperature.
- Prior to localization – all materials have quite similar characteristics of the perturbed fields. Yet, a large difference exists in the final number of shear bands which eventually evolve in the different materials.

Stage 2 – Shear bands initiation

- The number of actually “activated” shear bands depends on the relation $((W_f - W_i)/W_i)$ which is related to plasticity mechanisms holding back and stalling the rate of shear band evolution. When $(W_f - W_i)/W_i$ is small, as for *Ti6Al4V*, shear bands which initiated earlier propagate at high velocities, causing a shielding effect at this early stage, deactivate neighboring potential initiation sites.
- Shear band velocities could be related to the relation $(W_f - W_i)/W_i$. Shear band velocities in *CP-Ti* and *Ti6Al4V* measured in Mercier and Molinari (1998) match this conclusion (reported velocities were ~ 150 m/s for *CP-Ti* and 450 m/s for *Ti6Al4V*).

Stage 3 – Shear band evolution

- The number of shear bands remains constant during the later stages of collapse (new shear bands do not evolve and the old ones do not “heal”).

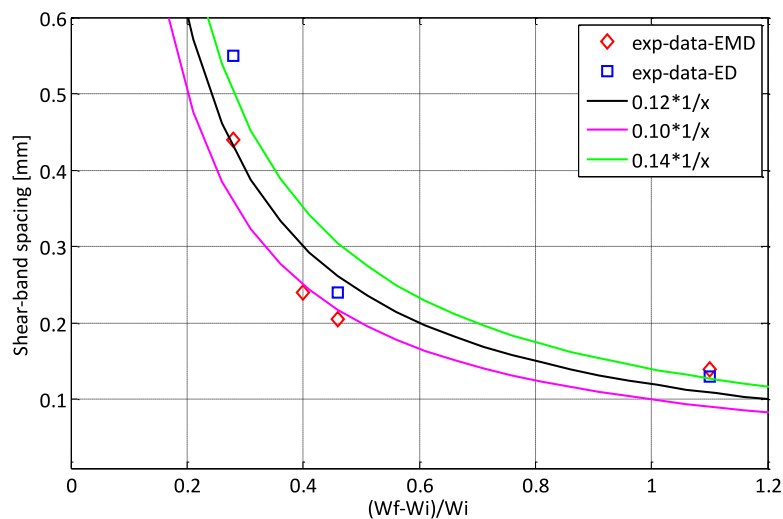


Fig. 16. Shear band spacing as a function of the normalized parameter $(W_f - W_i)/W_i$ (ED = Explosively driven, EMD = Electro-magnetically driven).

- The shear bands propagate in a competitive growth dominated by “shielding effects”, which is caused by release waves emanating from the developed shear bands. The later propagating shear bands which enter the released stress areas come to an earlier stop and have shorter lengths.

5. Summary and conclusions

In this work we carried out a 2D numerical study to explore the complex dynamics of spontaneous shear band evolution in collapsing thick walled cylinders. The numerical results provided a better comprehension for the different stages of shear band formation and a reliable description of the shear band distributions and spacing, paving the way for predictive work. Calibration of the failure model, based on a strain energy density criterion for four different materials, resulted in good *quantitative* comparison with the experimental results.

The ratio $(W_f - W_i)/W_i$ in the strain energy density model, referring to the rate of localization, is related to plasticity mechanisms which may hold back and stall the rate of shear band evolution. Given a technique to measure W_i and W_f , or the difference $W_f - W_i$, which is possibly related to shear band velocity, spacing could be quantitatively predicted for any material. Numerical simulations using the energy density failure model were proved to be a powerful tool to explore the physics of spontaneous shear localization in collapsing thick walled cylinders.

Acknowledgments

The financial support of the Israel Science Foundation – ISF (Grant 1034/13) and of the Pazy Foundation (Grant 2021077) is kindly acknowledged.

References

- Areias, P.M.A., Belytschko, T., 2007. Two-scale method for shear bands: thermal effects and variable bandwidth. *Int. J. Numer. Methods Eng.* 72, 658–696.
- Coghe, F., Tirry, W., Rabet, L., Schryvers, D., Van Houtte, P., 2012. Importance of twinning in static and dynamic compression of a Ti6Al4V titanium alloy with an equiaxed microstructure. *Mater. Sci. Eng. A* 537, 1–10.
- Cox, D.R., Oakes, D., 1984. *Analysis of Survival Data*. Chapman & Hall, London.
- Daridon, L., Oussouaddi, O., Ahzi, S., 2004. Influence of the material constitutive models on the adiabatic shear band spacing: mts, power law and JC models. *Int. J. Solids Struct.* 41, 3109–3124.
- Davidenkova, N., Miroslubov, I., 1935. *Tech. Phys. USSR* 2, 281.

- Dodd, B., Walley, S.M., Yang, R., Nesterenko, V.F., 2015. Major steps in the discovery of adiabatic shear bands. *Metall. Mater. Trans. A* 46 (10), 4454–4458.
- Dolinski, M., Merzer, M., Rittel, D., 2015. Analytical formulation of a criterion for adiabatic shear failure. *Int. J. Impact Eng.* 85, 20–26.
- Dolinski, M., Rittel, D., Dorogoy, A., 2010. Modeling adiabatic shear failure from energy considerations. *J. Mech. Phys. Solids* 58, 1759–1775.
- Firstenberg, O., Ashuach, Y., Partom, Y., 2006. A simple model for dynamic shear failure of stainless steel. 8th Int. Conference on Mechanical and Physical Behaviour of Materials under Dynamic Loading. *J. Phys. IV France* 134, 191–196.
- Follansbee, P.S., Kocks, U.F., 1988. A constitutive description of the deformation of copper based on the use of the mechanical threshold stress as an internal state variable. *Acta Metall.* 36, 82–93.
- Grady, D.E., 1982. Local inertial effects in dynamic fragmentation. *J. Appl. Phys.* 53 (1), 322–325.
- Johnson, G.R., Cook, W.H., 1983. A constitutive model and data for metals subjected to large strains, high strain rates and high temperatures. In: *Proceedings of 7th International Symposium on Ballistics*, pp. 12–21.
- Kravt-Tarnavskii, V.P., 1928. A peculiar band discovered in steel (in Russian). *J. Russ. Metall. Soc.* 3, 162.
- Lovinger, Z., Partom, Y., 2009. Simulation of multiple shear bands in collapsing cylinder experiments. In: *Proceedings of the 8th International Conference on Mechanical and Physical Behaviour of Materials under Dynamic Loading*. DYMAT, pp. 1649–1656.
- Lovinger, Z., Rikanati, A., Rosenberg, Z., Rittel, D., 2011. Electro-magnetic collapse of thick walled cylinders to investigate spontaneous shear localization. *Int. J. Impact Eng.* 38, 918–929.
- Lovinger, Z., Rittel, D., Rosenberg, Z., 2015. An experimental study on spontaneous adiabatic shear band formation in electro-magnetically collapsing cylinders. *J. Mech. Phys. Solids* 79, 134–156.
- Medyanik, S.N., Liu, W.K., Li, S., 2007. On criteria for dynamic adiabatic shear band propagation. *J. Mech. Phys. Solids* 55, 1439–1461.
- Mercier, S., Molinari, A., 1998. Steady state shear band propagation under dynamic conditions. *J. Mech. Phys. Solids* 46 (8), 1463–1495.
- Meyers, M.A., Xu, Y.B., Xue, Q., Perez-Prado, M.T., McNelly, T.R., 2003. Microstructural evolution in adiabatic shear localization in stainless steel. *Acta Mater.* 51, 1307–1325.
- Molinari, A., 1997. Collective behavior and spacing of adiabatic shear bands. *J. Mech. Phys. Solids* 45 (9), 1551–1575.
- Noam, T., Dolinski, M., Rittel, D., 2014. Scaling dynamic failure: a numerical study. *Int. J. Impact Eng.* 69, 69–79.
- Osovski, S., Rittel, D., Landau, P., Venkert, A., 2012. Microstructural effects on adiabatic shear band formation. *Scr. Mater.* 66 (1), 9–12.
- Rabczuk, T., Samaneigo, E., 2008. Discontinuous modelling of shear bands using adaptive meshfree methods. *Comput. Methods Appl. Mech. Eng.* 197, 641–658.
- Rittel, D., Landau, P., Venkert, A., 2008. Dynamic recrystallization as a potential cause for adiabatic shear failure. *Phys. Rev. Lett.* 101, 165501.
- Rittel, D., Wang, Z.G., Merzer, M., 2006. Adiabatic shear failure and dynamic stored energy of cold work. *Phys. Rev. Lett.* 96, 075502.
- Rodriguez-Martinez, J.A., Rusinek, A., Pesci, R., Zaera, R., 2013. Experimental and numerical analysis on the martensitic transformation in AISI 304 steel sheets subjected to perforation by conical and hemispherical projectiles. *Int. J. Solids Struct.* 50 (2), 339–351.
- Steinberg, D.J., Cochran, S.G., Guinan, M.W., 1980. A constitutive model for metals applicable at high strain rate. *J. Appl. Phys.* 51, 1498–1504.

- Triantafyllidis, N., Waldenmyer, J.R., 2004. Onset of necking in electro-magnetically formed rings. *J. Mech. Phys. Solids* 52, 2127–2148.
- Wilkins, M.L., 1964. Calculation of elastic-plastic flow. In: Alder, B., Fernbach, S., Rotenberg, M. (Eds.), *Methods in Computational Physics* V3. Academic press, New York, pp. 211–263.
- Wright, T.W., Okendon, H., 1996. A scaling law for the effect of inertia on the formation of adiabatic shear bands. *Int. J. Plast.* 12 (7), 927–934.
- Xue, Q., Meyers, M.A., Nesterenko, V.F., 2002. Self Organization of shear bands in titanium and Ti-6Al-4 V alloy. *Acta Mater.* 50, 576–596.
- Xue, Q., Meyers, M.A., Nesterenko, V.F., 2004. Self Organization of shear bands in steel. *Mater. Sci. Eng. A* 384, 35–46.
- Yang, Y., Li, D.H., Zheng, H.G., Li, X.M., Jiang, F., 2009. Self organization behavior of shear bands in 7075-T73 and annealed aluminum. *Mater. Sci. Eng. A* 527, 344–354.
- Yang, Y., Zeng, Y., Gao, Z.W., 2008. Numerical and Experimental studies of self-organization of shear bands in 7075 aluminum alloy. *Mater. Sci. Eng. A* 496, 291–302.
- Zener, C., Hollomon, J.H., 1943. Effect of strain rate upon plastic flow of steel. *J. Appl. Phys.* 15, 22–32.